

Quantum transport in nitrogen-doped nanoporous graphenes

Gaetano Calogero^{1†}, Isaac Alcón^{2,3†*}, Alan E. Anaya Morales⁴, Nick Papior⁵, Pol Febrer², Aron W. Cummings², Miguel Pruneda^{2,6}, Stephan Roche^{2,7} and Mads Brandbyge⁴

¹*National Research Council, Institute for Microelectronics and Microsystems (CNR-IMM), Zona Industriale, Strada VIII, 5, 95121 Catania, Italy*

²*Catalan Institute of Nanoscience and Nanotechnology (ICN2), CSIC and BIST, Campus UAB, Bellaterra, 08193 Barcelona, Spain*

³*Institute of Theoretical and Computational Chemistry, Department of Materials Science and Physical Chemistry, Universitat de Barcelona, C/ de Martí i Franquès, 1-11, Les Corts, 08028, Barcelona, Spain*

⁴*Department of Physics, Technical University of Denmark, DK-2800 Kongens Lyngby, Denmark*

⁵*Computing Center, Technical University of Denmark, DK-2800 Kongens Lyngby, Denmark*

⁶*Nanomaterials and Nanotechnology Research Centre (CINN-CSIC), Universidad de Oviedo (UO), Principado de Asturias, 33940 El Entrego, Spain*

⁷*ICREA, Institució Catalana de Recerca i Estudis Avançats, 08070 Barcelona, Spain*

[†]equally contributed

*Corresponding author: ialcon@ub.edu

Abstract

Bottom-up on-surface synthesized nanoporous graphenes (NPGs), realized as 2D arrays of laterally covalently bonded π -conjugated graphene nanoribbons (GNRs), are a family of carbon nanomaterials which are receiving increasing attention for nanoelectronics and biosensing. Recently, a so-called hybrid-NPG (hNPG) was synthesized, featuring an alternating sequence of doped and non-doped GNRs, resulting in a band staggering effect in its electronic structure. Such a feature is appealing for photo-catalysis, photovoltaics and even carbon nanocircuitry. However, to date, little is known about the transport properties of hNPG and its derivatives, which is key for most applications. Here, via Green's functions simulations, we study the quantum transport properties of hNPGs. We find that injected carriers in hNPG spread laterally through a number of GNRs, though such spreading may take place exclusively through GNRs of one type (doped or non-doped). We propose a simple model to discern the key parameters determining the electronic propagation in hNPGs and explore alternative hNPG designs to control the spreading/confinement and anisotropy of charge transport in these systems. For one such design, we find that it is possible to send directed electric signals with sub-nanometer precision for as long as one micrometer – a result first reported for any NPG.

Introduction

The power of bottom-up on-surface synthesis to realize virtually any carbon nanostructure has been demonstrated during the last two decades.^{1–3} While a number of nanomaterials have been reported in this way, including 2D covalent organic frameworks¹ and molecular nanographenes,^{4,5} only graphene nanoribbons (GNRs) have acquired major attention for nanoelectronics.^{6,7} This is partly due to their fully π -conjugated nature and semiconducting band structure, which opens the door to control current flow through such nanomaterials via electrostatic means. In spite of the significant amount of research devoted to GNR-based devices, there are still major challenges, such as controlling the length of bottom-up synthesized GNRs or their arrangement within solid-state devices.⁷ The so-called nanoporous graphenes (NPGs) are GNR-based 2D materials that could solve some of these issues. NPGs, first reported in 2018,⁸ are 2D covalent arrays of laterally bonded GNRs, and so they may be regarded as a 2D net of electronically coupled 1D nanochannels for charge carriers.⁹ Different types of NPGs have been synthesized since then, by varying the GNR type (including arm-chair, chevron like, etc.) or the covalent linkage between the ribbons, including direct C-C bonding or molecular bridges.¹⁰ While NPG research is still in the early stages, some researchers have managed to integrate them in solid-state devices.^{8,11}

One of the most recent members of the NPG family of materials is the so-called hybrid-NPG (hNPG for short).¹² The hNPG is formed by 7-13 arm-chair GNRs (7-13-AGNRs), as for the original NPG,⁸ but every other GNR in hNPG is nitrogen-doped (N-doped), making the hNPG a 2D array of alternating N-doped GNRs (nGNRs hereafter) and non-doped GNRs (cGNRs), as depicted in Fig. 1a-b. Such chemical alternation gives rise to a type II band-staggering effect,¹² where the valence band of the material originates from cGNRs and the conduction band originates from the nGNR array (see Fig. 1c). As such, hNPG is a lateral heterojunction with atomically sharp band offsets alternating on the nanometer scale, which makes it a relevant platform for applications in optoelectronics, photovoltaics, photocatalysis and selective ion sieving.¹² However, hNPG also displays in-gap tunnelling states in the energy range spanned by the valence (conduction) band that couple all cGNRs (nGNRs) through nGNRs (cGNRs), as schematically represented in Fig. 1c (see “tunneling states”). The existence of these in-gap tunneling states could hinder the lateral confinement of electron propagation and limit spatial control.

In this work, we study the quantum transport properties of hNPG and its derivatives. We do this via density functional theory (DFT) combined with the Green's function (GF) formalism. Concretely, we simulate the application of gates to set the Fermi energy (E_F) either within the valence or conduction band of hNPG, which allows us to evaluate the behavior of injected currents upon locally probing either a cGNR or a nGNR. We find that the band staggering effect does not prevent the lateral spreading of locally injected currents, which we associate with the presence of tunneling states that become more pronounced upon gating. Inspired by former work on Talbot interference in NPGs,¹³ we develop an analytical model to describe the current propagation patterns emerging in hNPG, in analogy to photons propagating in coupled waveguides. We then investigate two design strategies towards transport confinement in hNPG-based systems. First, inspired by prior studies,¹² we consider alternative hNPG lateral distributions where a cGNR is separated from the next cGNR by an increasing number of nGNRs. Second, we combine the alternating doping of hNPG with the use of phenyl rings to bridge neighboring GNRs in meta-configuration, which, as previously studied in depth,^{10,14–16} leads to

destructive quantum interference (QI) effects and strong lateral confinement of charge carriers. While both strategies significantly reduce spreading of currents as compared to hNPG, we find that only the second route leads to full confinement of injected currents within the single contacted GNR. In the second scenario, we demonstrate that by tuning the gate voltage, the injected charge carriers can stay within a single GNR for more than one micrometer away from the injection point. Such level of control over current flow at the nanoscale represents a clear improvement over QI-based strategies alone, and demonstrates a synergistic effect upon combining QI and band-staggering engineering.

Results and discussion

Figure 1a displays the optimized structure of hNPG, built as a lateral heterostructure of (N-doped) nGNRs and (non-doped) cGNRs laterally connected via single C-C bonds. As previously mentioned, such N-doping leads to an energetic stabilization of nGNR states with respect to cGNR states.¹² As a consequence, the valence band consists nearly entirely of cGNR orbitals, whereas the conduction band is made up of nGNR orbitals, as shown by the GNR-resolved fat band structure in Fig. 1d. Similar to other NPGs, both the valence and conduction bands are primarily dispersive along the GNRs (x-direction; $\Gamma \rightarrow X$), indicative of their conductive character. However, in Fig. 1d we also see a non-negligible band dispersion across the GNRs ($\Gamma \rightarrow Y$ segment), which indicates a certain degree of electronic coupling between GNRs of the same type. As previously reported,¹² such finite coupling originates from the presence of tunnelling states, which may be observed in the y-resolved local density-of-states (LDOS) shown in Fig. S1 of the Supporting Information (SI).

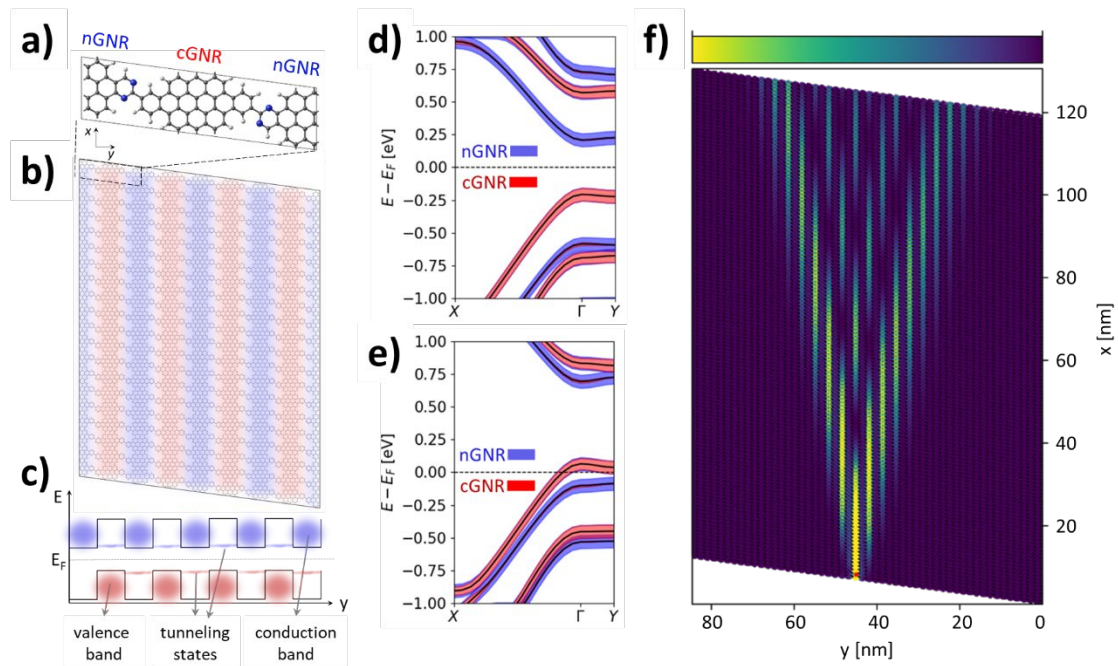


Fig. 1. a) Optimized atomic structure of hNPG (C: grey, N: blue, H: white). b) Medium-scale atomistic model of hNPG. c) Outline of the type II band staggering in hNPG, where the valence and conduction bands are highlighted in red and blue, respectively. Tunneling states are also highlighted with the same color scheme as the GNR type. d) GNR-resolved fat band structure (cGNR: red; nGNR: blue) for the charge-neutral system and e) the $-0.89 \cdot 10^{13} \text{ e/cm}^2$ p-gated system (-0.25 e/cell). f) Bond transmission maps of a $\sim 85 \times 122 \text{ nm}^2$ hNPG sample gated as in e), upon locally contacting the central cGNR at the bottom of the device (see small red dot). Areas with high bond transmission are shown in bright yellow, those with low or no bond transmission are in dark (color bar ranging from 0 to 0.045).

The band structure of hNPG suggests that, in principle, positive charge carriers should exclusively propagate through cGNR states (setting $E - E_F$ within the valence band) and negative charge carriers through nGNR states (setting $E - E_F$ within the conduction band). To assess this, we use the GF method to simulate the local injection of charge in hNPG devices electrostatically gated with either holes or electrons (see Methods for details). We systematically increase the gate both for holes and electrons from 0.1 e/cell to 1 e/cell, which approximately correspond to 0.36×10^{13} and 3.6×10^{13} e/cm², respectively, which are experimentally attainable (e.g. in graphene).¹⁷ We note that such concentrations are experimentally attainable in graphene.¹⁸ Gating leads to a narrowing of the energy spacing between the cGNR band onset and the nGNR band onset, both for valence and conduction bands (see Figs. 1e and S2), thus making the hNPG look more like the “original” NPG. Such behavior may be understood as follows. Taking p-gating as an example, emptying the valence band leads to an effective positive charging of cGNRs, due to the primary cGNR character of the valence band. Such positive charging stabilizes cGNR states with respect to nGNR states, due to a lower Coulomb repulsion, thus shifting the onset energies of the respective bands closer to each other. For n-gating the opposite phenomenon occurs: nGNRs are increasingly filled with electrons (due to the primarily nGNR character of the conduction band) which become negatively charged, increasing Coulomb repulsion and thus their relative energy with respect to cGNRs. This narrowing of the gap between cGNR and nGNR bands reduces the range of gate voltages for which E_F exclusively crosses either the cGNR band (-0.89×10^{13} e/cm²) or the nGNR band (0.89×10^{13} e/cm²), as shown in Fig. S2. In Fig. 1e we display the band structure for the p-gated case, which will be used to illustrate the transport properties of hNPG.

To evaluate quantum transport in hNPG, we take the p_z elements of the DFT Hamiltonian to build an effective tight binding (TB) model that captures the hNPG electronic structure under the effect of electrostatic gates (see Methods for details). This TB representation is then used to build a large-scale hNPG device composed of 291,200 atoms, in which we simulate local injection of charge under a -0.89×10^{13} e/cm² p-gate (see associated band structure in Fig. 1e). As seen in Fig. 1f, local injection at the bottom region of the central cGNR leads to significant charge spreading, even upon setting E_F to only cross the valence band with primarily cGNR character. This demonstrates that the band staggering of hNPG is not sufficient to confine injected currents to a single GNR, which we associate to the presence of tunneling states (Figs. 1c and S1). We see, however, that the resulting Talbot interference, typical for NPGs,¹³ displays an alternating pattern; that is, the bond transmission amplitude exclusively emerges in the cGNRs with nearly no amplitude in the nGNRs. This is a unique feature of hNPG which originates from the primarily cGNR character of the valence band that is electrically probed (see Fig. 1e). If we locally contact an nGNR, we observe a significant reduction of the overall transmission amplitude (Fig. S3c) which may be associated with the smaller contribution of nGNR states at E_F under the applied -0.89×10^{13} e/cm² p-gate (see associated LDOS in Fig. S4). Exactly the opposite scenario is obtained upon applying the corresponding n-gate ($+0.89 \times 10^{13}$ e/cm²), which populates the nGNR conduction band (Fig. S5a): namely, the emergence of a nGNR-hosted Talbot interference pattern upon locally contacting a nGNR (Fig. S5c) and the near absence of transmission amplitude upon contacting a cGNR (Fig. S5b). Further increasing the gate voltage (either positive or negative) simultaneously populates both cGNR and nGNR bands, leading to a superposition of two Talbot interference patterns that emerge, with equal intensity, regardless of the contacted GNR (see Figs. S6 and S7 associated to $-3.58 \cdot 10^{13}$ e/cm² and $+3.58 \cdot 10^{13}$ e/cm² gates, respectively). These two superimposed Talbot patterns are associated with the electronic wave functions of the two GNR subsystems (i.e. cGNRs and nGNRs; see below).

The results in Fig. 1 clearly show that the band staggering of hNPG is insufficient to achieve confinement of currents in single GNRs. To better understand such complex transport behavior and propose directions to achieve current confinement, we propose a simple analytical model capturing the essential electronic features observed for hNPG (full details in Methods). This framework generalizes the Talbot interference model presented in Ref. 13, which was based on an analogy between GNRs in NPGs and the channels within an array of laterally coupled optical waveguides. Here, the alternating sequence of nGNRs and cGNRs is represented by a periodic array of coupled waveguides labeled A_n and B_n , respectively, with n denoting the unit cell index in the y direction (Fig. 2a). Each waveguide supports a single propagating mode with a local energy shift (propagation constant), ϵ_A and ϵ_B . We assign $\epsilon_A = -\alpha$ and $\epsilon_B = \alpha > 0$, explicitly incorporating the band staggering observed in hNPG, and define κ as the coupling constant between waveguides. In the optical analogy, α mimics a refractive index contrast, while κ corresponds to the evanescent coupling between neighboring waveguides.

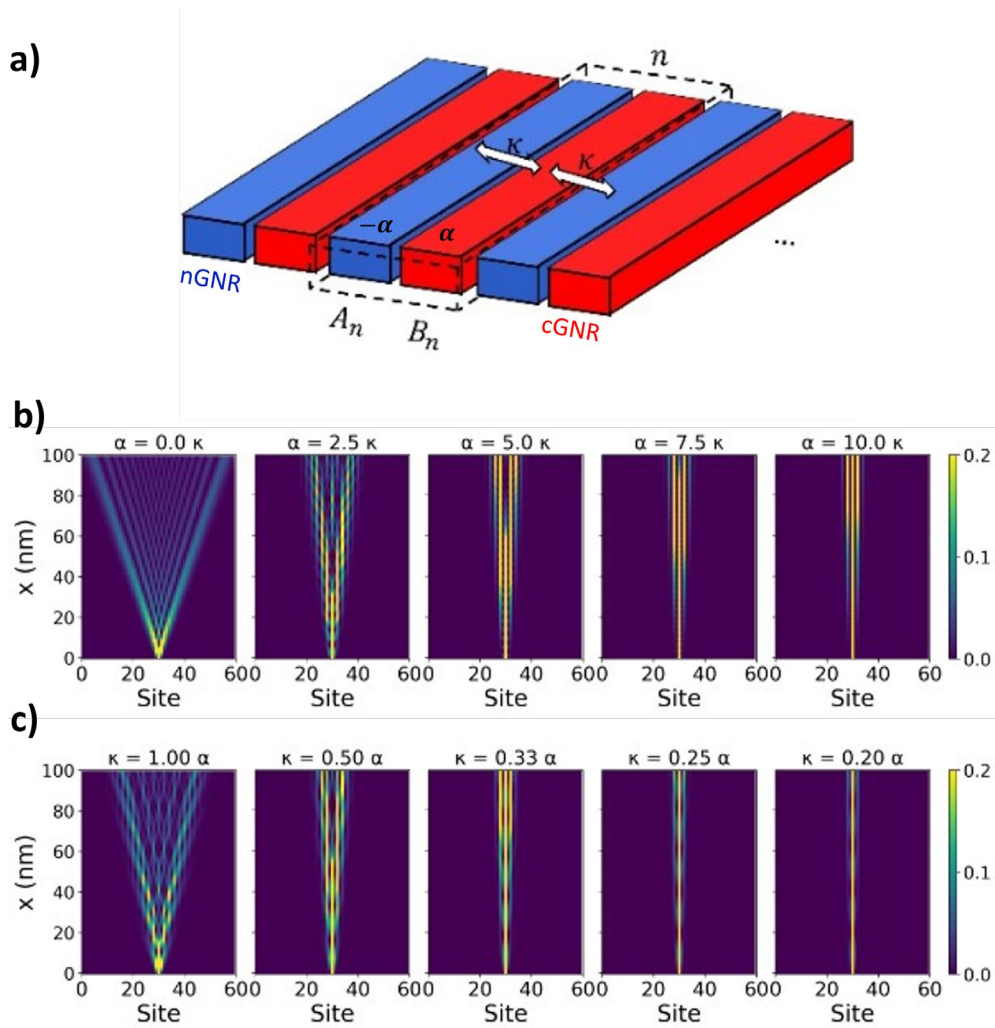


Fig. 2. a) Schematic of the model representing hNPG as an infinite array of alternating A_n (B_n) waveguides with potential propagation constant $-\alpha$ (α), weakly coupled to their nearest neighbor by κ , with n the unit cell index in the y -direction. b) Spatial propagation of waveguide amplitude obtained with the waveguide model for increasing values of the propagation constant (α) at a fixed $\kappa = 0.014 \text{ \AA}^{-1}$. c) Spatial propagation of waveguide amplitude for decreasing coupling κ at fixed $\alpha = 0.065 \text{ \AA}^{-1}$.

In Fig. 2b, we show the propagating wave modes for increasing α/κ , while fixing $\kappa = 0.014 \text{ \AA}^{-1}$. The results exhibit a range of interference behavior, from the Talbot regime ($\alpha = 0$) to strong localization to ~ 3 ribbons ($\alpha = 10\kappa$). At intermediate values of α/κ , pronounced beating patterns in the cGNR waveguides (B_n) are observed. Strong (but not yet complete) localization of the field intensity along the contacted nGNR (A_0) is achieved only for large values of $\alpha \gg 10\kappa$, which may be challenging to achieve solely by chemical means. However, localization can also be achieved by combining the effects of moderate band staggering and reduced inter-ribbon coupling. This is demonstrated in Fig. 2c, where the propagating modes are shown for increasing α/κ , fixing $\alpha = 0.065 \text{ \AA}^{-1}$. For $\kappa = \alpha$, field intensities exhibit large spreading, albeit less pronounced than in NPG, due to the finite value of α . In this intermediate regime, $\kappa \sim \alpha$, field intensities cannot be described by Talbot-interference. As κ decreases further, confinement is noticeably enhanced (see right panels in Fig. 2c).

In light of these results, below we explore alternative hNPG designs to reduce the inter-ribbon coupling κ and achieve fully confined charge propagation in the GNRs, which is of high interest for carbon nanocircuitry and, more generally, carbon nanoelectronics. Following prior proposals,¹² we first consider hNPG structures where every cGNR is surrounded by an increasing number of nGNRs, which should lead to a depletion of tunneling states and a reduced inter-cGNR coupling. More specifically, we consider hNPGs where cGNRs, instead of being separated by one nGNR as in hNPG (see Fig. 1a), are separated by two nGNRs (hNPG-1,2, Fig. 3a), three nGNRs (hNPG-1,3, Fig. 3c) or four nGNRs (hNPG-1,4, Fig. 3e). In this notation (hNPG-p,q) p and q are the number of cGNRs and nGNRs within the unit cell, respectively. In order to exploit the isolation of cGNR states to achieve 1D confinement, one needs to set E_F to cross only the cGNR valence band. As done for hNPG, this requires a p-gate of ca. $-0.90 \cdot 10^{13} \text{ e/cm}^2$ (see Fig. 1e), which we thus apply to hNPG-1,2, hNPG-1,3 and hNPG-1,4 during the optimization of the atomic and electronic structure (see Methods for details). To evaluate the effectiveness of these hNPG derivatives to confine currents, we simulate the injection of charge for the corresponding large-scale devices, locally probing the bottom region of the central cGNR. As we may see in Fig. 3b, separating cGNRs by two nGNRs indeed leads to a lower degree of current spreading as compared to hNPG (Fig. 1f), which is associated with an effective decrease of inter-cGNR coupling. By looking at the associated GNR-resolved fat band structure (Fig. 3a), we see that hNPG-1,2 displays two nGNR bands near E_F arising from the two nGNRs present in the hNPG-1,2 unit cell (see zoomed band structure). Such bands, by contributing to the y-resolved LDOS at such a doping level (Fig. S8), prevent a clean interrogation of cGNR states at E_F . Upon including more nGNRs in the unit cell, additional nGNR bands appear in the band structure nearby E_F or even crossing it, as shown in Figs. 3c and 3e for hNPG-1,3 and hNPG-1,4, respectively, and reflected in the associated LDOS (Fig. S8). Therefore, upon adding more nGNRs it gets increasingly difficult to set E_F within the longitudinal regime of the cGNR valence band (that is, injecting carriers with a net momentum within the $\Gamma \rightarrow X$ segment) while preventing E_F from crossing such emergent nGNR bands. As a consequence, despite the higher degree of confinement achieved by moving from hNPG (Fig. 1f) to hNPG-1,4 (Fig. 3f), which increases the physical separation between cGNRs, there appear leaking currents due to such “new” nGNR bands near E_F . This effect, which is particularly evident for hNPG-1,3 and hNPG-1,4 (Figs. 3d and 3f, respectively), makes it challenging to control current flow with atomic precision in such hNPG-based lateral heterostructures .

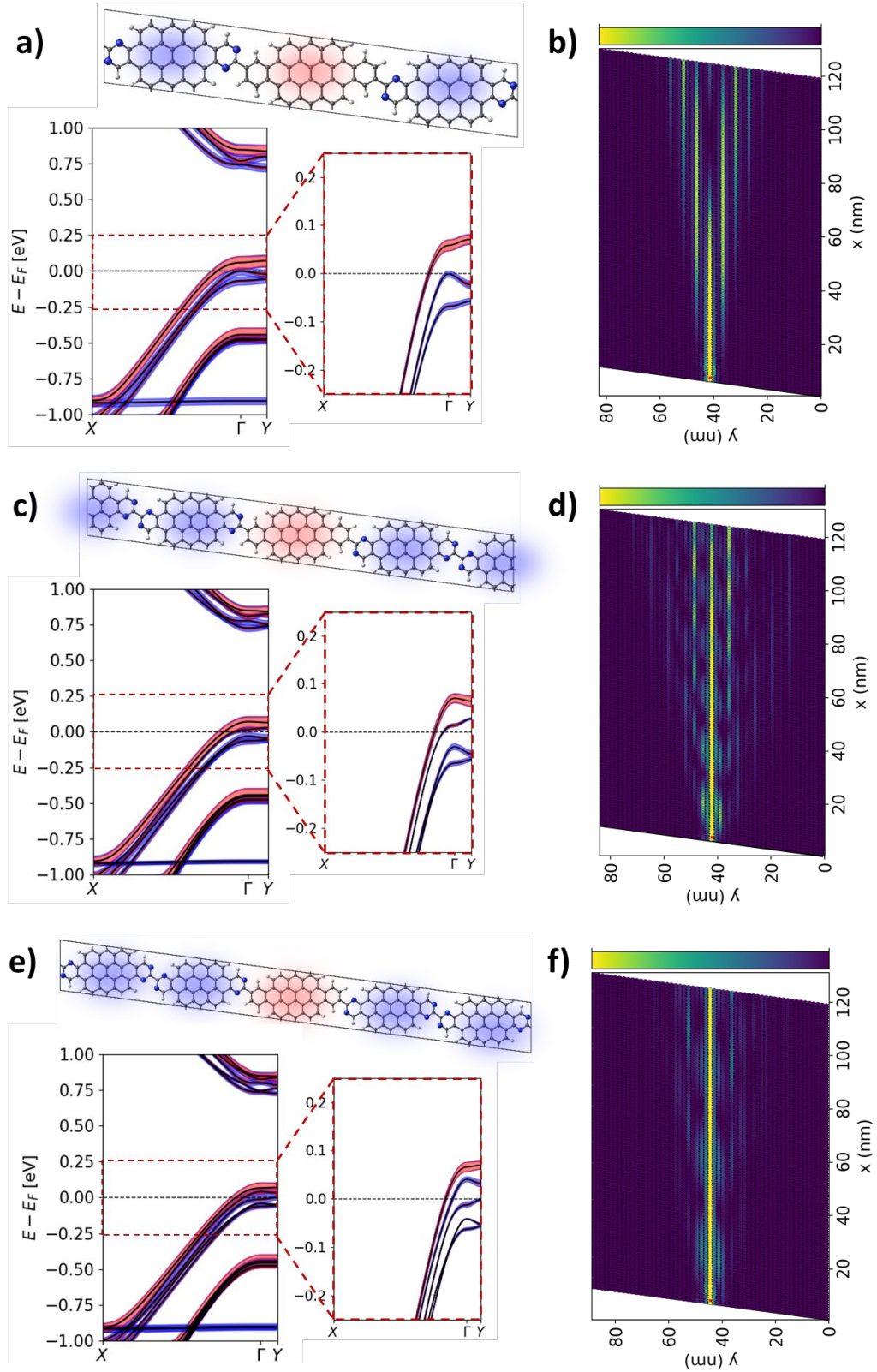


Fig. 3. hNPG derivatives separating every cGNR, highlighted in red, by a) two nGNRs (hNPG-1,2), c) three nGNRs (hNPG-1,3) and e) four nGNRs (hNPG-1,4), highlighted in blue. All systems have been optimized under a p-gate of $-0.90 \cdot 10^{13} \text{ e/cm}^2$. Below each geometry the associated GNR-resolved fat band structure (cGNR: red; nGNR: blue) is shown, along with a zoomed view around E_F . Associated bond transmission maps of $\sim 85 \times 122 \text{ nm}^2$ samples contacted in the bottom region of the central cGNR (see small red dot) are shown in b) hNPG-1,2 (285,600 atoms), d) hNPG-1,3 (291,200 atoms) and f) hNPG-1,4 (308,000 atoms). All color bars in the bond transmission maps range from 0 to 0.045.

As a second strategy, we evaluate the use of QI in hNPGs. QI has been previously shown to be an effective route to engineer the transport properties of NPGs even under strong electrostatic¹⁵ or dynamic (thermal) disorder.¹⁶ To incorporate QI in the hNPG framework we connect every GNR with its neighbors via phenyl rings in meta-configuration, giving rise to a new NPG whose geometry is shown in Fig. 4a, which we label meta-hNPG. As seen in Figs. 4b-c, the GNR contributions to the band structure in meta-hNPG are similar to those in hNPG (Fig. 1d) – namely, the valence states are primarily localized in cGNRs and the conduction states in nGNRs (Fig. 4c). However, the LDOS (Fig. 4b) and GNR-resolved partial density of states (Fig. S9) highlight a significant difference. For hNPG, in the valence (conduction) band energy range there is a non-negligible contribution by nGNR (cGNR) states (see arrows in Fig. S9c) associated with tunneling states (Fig. S9b). On the contrary, in meta-hNPG such contributions are absent for both the valence and conduction bands (Fig. S9f), which we associate with the absence of tunneling states (Fig. 4b). The suppression of tunneling states in this material upon gating is also confirmed (compare Fig. S10 with Fig. S4).

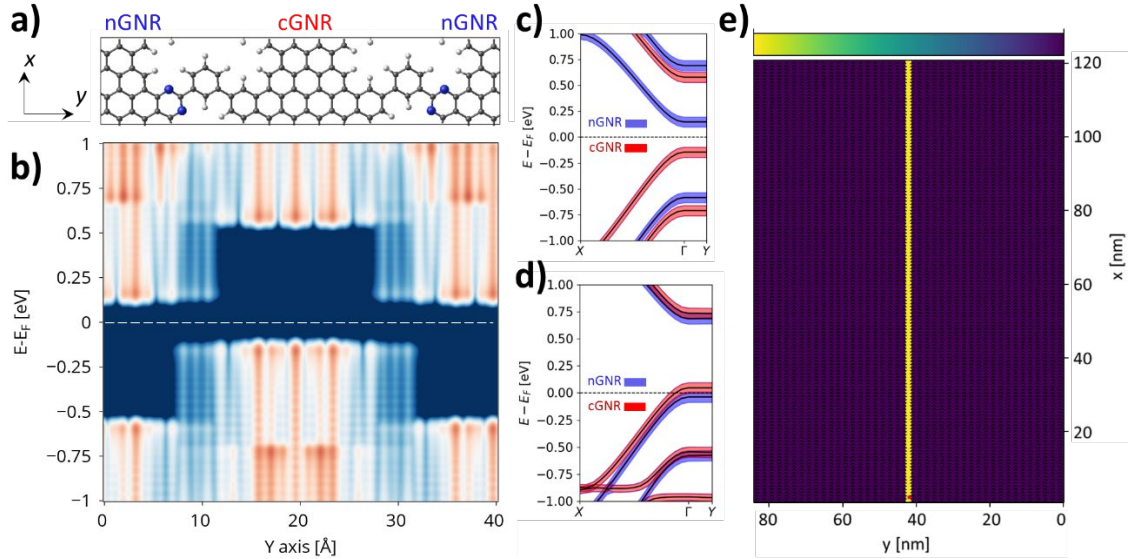


Fig. 4. a) Optimized geometry of meta-hNPG and corresponding (b) y -resolved LDOS. The colors are in a log scale, with dark red (blue) indicating a high (low) LDOS. E_F is indicated with a dashed white line. Associated GNR-resolved fat band structure (cGNR: red; nGNR: blue) for c) the charge-neutral meta-NPG and d) the $-0.72 \cdot 10^{13} \text{ e/cm}^2$ p -gated material (-0.25 e/cell). e) Bond transmission map of a $\sim 85 \times 122 \text{ nm}^2$ sample of the p -gated meta-hNPG upon locally contacting the central cGNR at the bottom region of the device (see small red dot). The color bar ranges from 0 to 0.045.

As already mentioned, such tunneling states are instrumental in hNPGs to enable the coupling between GNRs of the same type and hence, ultimately, for the spreading of currents across GNRs. This relation seems to hold for meta-hNPG, displaying a negligible band dispersion in the $\Gamma \rightarrow Y$ path of the Brillouin zone (Fig. 4c) and, simultaneously, a lack of tunneling states (Fig. 4b). To evaluate the transport properties of meta-hNPG we focus on the p -gated system under a gate of -0.25 e/cell (as for hNPG) corresponding to $-0.72 \cdot 10^{13} \text{ e/cm}^2$. As may be seen in the corresponding band structure (Fig. 4d) and LDOS (Fig. S10), this gate positions E_F within the top valence band, primarily of cGNR character. By locally injecting currents in a large-scale meta-hNPG sample, shown in Fig. 4e (270,480 atoms), we see that full confinement of carriers is achieved within the single contacted cGNR up to at least 120 nm from the injection point (see small red dot at the bottom region of the sample). Similar to hNPG (Fig. S3), probing an nGNR gives rise to no transmission (Fig. S11). Increasing the applied gate (-0.5 e/cell) sets E_F to cross

both cGNR and nGNR bands (Fig. S12a) but, remarkably, full confinement of currents is still obtained regardless of the contacted GNR (Fig. S12b-c). Such level of collimation, well beyond both the hNPG (Fig. 1f) and its lateral heterostructures (Fig. 3), highlights the power of QI-engineering as a tool to control current flow in these nanomaterials.

The extremely efficient current confinement in meta-hNPG leads to the natural question of how it compares to bare QI-engineering strategies applied to NPGs without band staggering, such as in the so-called meta-NPG.¹⁴ Meta-NPG has exactly the same geometry as meta-hNPG, but is composed entirely of cGNRs. Consequently, in meta-NPG all GNRs are energetically degenerate, and hence current confinement solely originates from QI effects (i.e. due to meta-configured phenyl bridges). Given the strongly localized nature of transport in both cases, to discern possible differences we simulate much longer devices (i.e. $\sim 45 \times 610 \text{ nm}^2$, containing 710,424 atoms) thus reaching the μm scale, and simulate the local injection of currents under a $-1.4 \cdot 10^{13} \text{ e/cm}^2$ p-gate (-0.5 e/cell). As shown in Fig. 5a, current spreading sets in for meta-NPG after $\sim 100 \text{ nm}$ from the injection point, monotonically increasing from that distance onwards. On the contrary, injected currents in meta-hNPG stay fully collimated within the single contacted cGNR up to 600 nm (Fig. 5b) and even $1 \mu\text{m}$ (Fig. S13), without showing any sign of spreading (see zoomed panels in Figs. 5b and S13a). Additionally, at this p-gate value, such effective collimation works equally well upon contacting an nGNR (Fig. S13b). Given the width of 7-13-AGNRs ($\sim 0.7 \text{ nm}$), our findings imply that one could send electric signals with sub-nanometer precision at least $1 \mu\text{m}$ away from the source using meta-hNPG-based carbon nanocircuits.

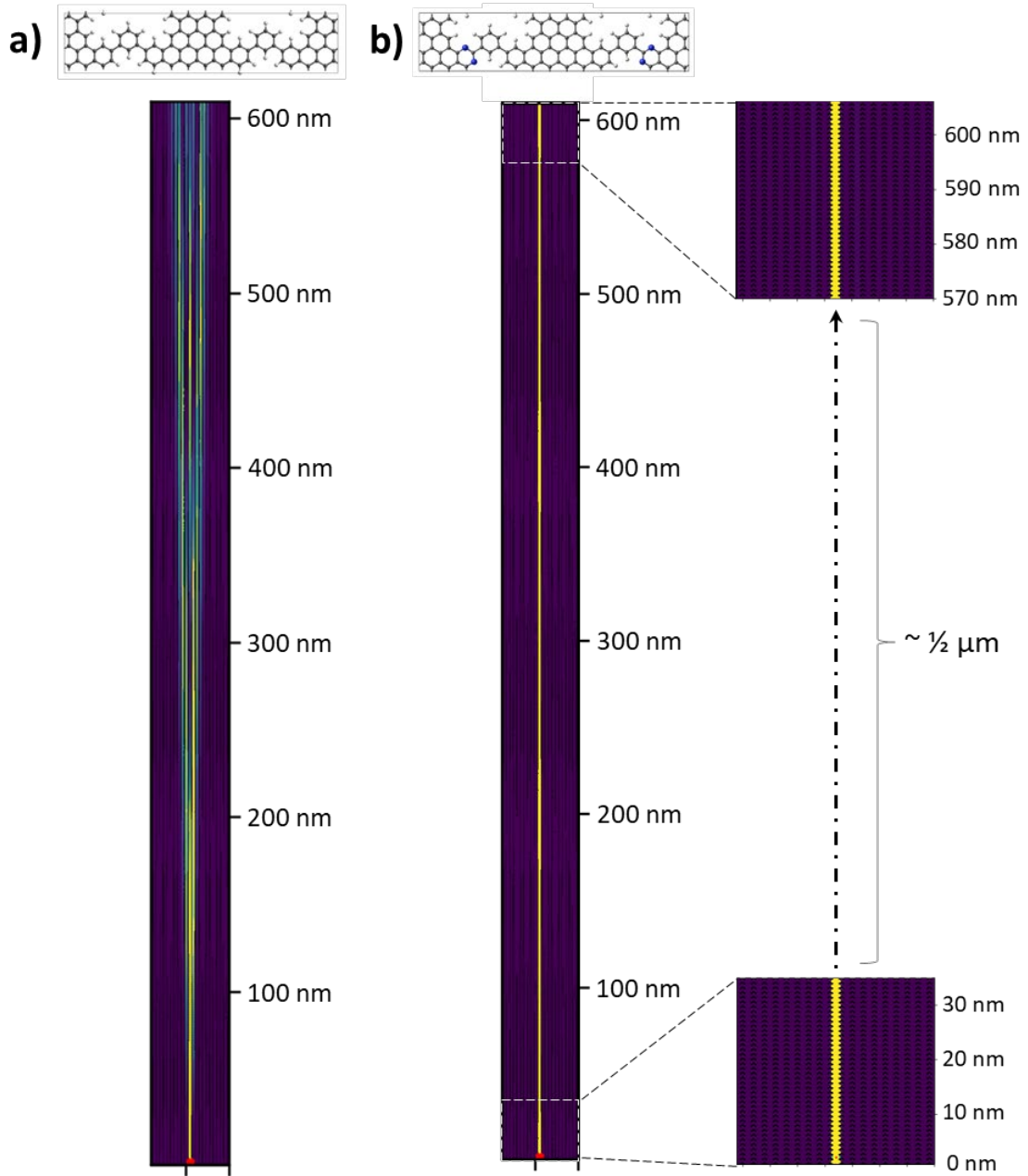


Fig. 5. Bond transmission maps of $-1.44 \cdot 10^{13} \text{ e/cm}^2$ p-gated a) meta-NPG and b) meta-hNPG samples, with a size of $45 \times 610 \text{ nm}^2$. In both cases, charge is injected locally in the central cGNR at the bottom region of the device (see small red dot). The corresponding optimized atomic geometries are provided in the top panels. For meta-NPG (a) the corresponding band structure is shown in Fig. S14c. For the meta-hNPG (b) zoomed bond transmission maps are provided for the bottom and top regions of the device. All color bars in the bond transmission maps range from 0 to 0.045.

We have found that such high confinement behavior in meta-hNPG appears to be gate dependent. For example, if we n-gate the material with $+0.5 \text{ e/cell}$ ($+1.44 \cdot 10^{13} \text{ e/cm}^2$), thus setting E_F within the conduction band, contacting a cGNR leads to a slight confinement degradation after 300 nm and to appreciable spreading of currents to the nearest and next-nearest neighbor cGNRs for distances around $1 \mu\text{m}$ away from the source point (Fig. S14a; note that such spreading occurs exclusively throughout cGNRs, as for hNPG). Curiously, contacting an nGNR at this same gate ($+1.44 \cdot 10^{13} \text{ e/cm}^2$) displays perfect current collimation up to one μm (Fig. S14b), which could be attributed to the electron-hole asymmetry in this material due to the

presence of N atoms. In any case, the overall confinement in such n-gated meta-hNPG is still well beyond that of meta-NPG under the same conditions, where a noticeable spreading of currents begins as close as 60 nm from the point of injection (Fig. S14c).

Conclusions

In this work we have studied the transport properties of hNPG systems, which are 2D arrays of alternating cGNRs and nGNRs. Transport simulations of hNPG have shown that injected currents significantly spread throughout the material, leading to the well-known Talbot interference pattern as reported in other NPGs.^{13,14} However, the band staggering in hNPG leads to current spreading through the cGNR sub-system, the nGNR sub-system, or both, depending on the applied gate and the contacted GNR. Such unique effects may be fully captured with an analytical model that exclusively considers two key parameters: i) the on-site energy difference between GNRs of different type (propagation constant, α) and ii) the effective coupling between neighbouring GNRs (κ). This provides a physical understanding of the observed interference phenomena in the staggered system. The model was parameterized and validated by linking α and κ to the hNPG electronic band structure from DFT, and reproducing the bond transmission maps obtained using the TB-GF approach. The model highlights that Talbot interference is hosted in every other ribbon of hNPG, featuring a beating pattern that depends solely on α , as discussed in the SI. The model also suggested that current confinement can be enhanced by decreasing the coupling constant κ or by significantly increasing the band staggering α . The latter could be achieved, for instance, by adsorption of functional groups near the pores or by substitution of N dopants with more electronegative species. However, without a concurrent decrease in κ , it would still not allow for full confinement.

Therefore, in the second part of the work we focused on evaluating possible alternative hNPG design strategies to reduce the inter-ribbon coupling. First, we considered increasing the number of nGNRs between cGNRs. However, this strategy leads to the emergence of new nGNR bands very close to, or even crossing, the Fermi level in the gated systems. This leads to parasitic current spreading, preventing full confinement of charge carriers in single GNRs, which is needed for nanoelectronic applications requiring nearly atomic precision. Nevertheless, we have presented an alternative strategy that solves these issues. This is based on embedding QI-effects in the hNPG by connecting every GNR with meta-configured phenyl ring bridges. In the resulting material, which we label meta-hNPG, tunnelling states are nearly absent, which leads to full confinement of injected currents within a single GNR. Further, we find that meta-hNPG represents a significant improvement in terms of current collimation over its predecessor, the deeply studied meta-NPG. This highlights a synergistic effect present in meta-hNPG, where a combination of the band-staggering profile and QI gives rise to a level of control over current flow which is not possible otherwise. Despite a certain dependence on the applied gate (p-gate vs. n-gate) and the contacted GNR (cGNR vs. nGNR), meta-hNPG allows one to send electric signals with sub-nanometer precision for distances up to at least one micrometer away from the injection point. This result, along with recent studies that have shown that QI-engineering of transport survives thermal and electrostatic disorder,^{15,16} makes meta-hNPG a very promising platform for future carbon nanocircuitry and, more generally, carbon nanoelectronics.

Methods

Density functional theory

The atomic and electronic structure of hNPGs has been optimized with density functional theory (DFT) using the PBE (GGA) exchange-correlation functional,¹⁹ a single- ζ basis set with 0.02 Ry energy shift, norm-conserving Troullier–Martins pseudopotentials, a real-space mesh cutoff of 400 Ry and a $51 \times 15 \times 1$ Monkhorst–Pack k-point mesh. The SIESTA software²⁰ has been used for all DFT calculations. Periodic geometries have been optimized until all forces were below 0.01 eV/Å, also minimizing cell parameters except the c-parameter (z-direction) which was kept fixed to avoid inter-layer interactions (50 Å). The external application of electrostatic gates was simulated by placing fixed charges on a plane parallel to the 2D material positioned 10 Å away. For every applied gate, the atomic structure and cell parameters of the system were fully optimized to account for any relaxation mechanisms caused by the addition or removal of charge. All post analysis, including fat-band structures, LDOS, PDOS and band structures, was done with SISL.²¹

Quantum transport simulations

Transport simulations were performed using a well-established parameterization approach for π -conjugated two-dimensional materials,^{10,13,14,22–26} by extracting the onsite and coupling parameters of p_z orbitals for all C and N atoms from the converged DFT Hamiltonians and overlap matrices. These parameters were used to parameterize computationally efficient tight binding (TB) models generated with the open-source SISL Python package.²¹ In particular, all DFT Hamiltonian elements involving p_z atomic orbitals of C and N atoms were exploited to construct the TB Hamiltonian. The resulting TB band structure is slightly misaligned with respect to the DFT one. To solve this, all onsite energies in the TB Hamiltonian were rigidly shifted to match the DFT mid-gap level of the neutral systems, the valence band edge of the p-gated systems or the conduction band edge of the n-gated systems. This reproduced the DFT band structure within the energy range of interest for the quantum transport simulations (see Fig. S15a), while retaining the full interaction range of the DFT basis set. Consequently, such lighter TB models capture the impact of sub-nanometer quantum dipoles, in-gap tunneling states, electrostatic gates and hydrogen passivation on the electronic structure. We note that including other orbitals from DFT into the TB Hamiltonian, such as N- d_{xz} and N- d_{yz} , slightly improves the match with DFT bands (see Fig. S15b) at the cost of reducing the computational efficiency and the maximum achievable device size. Large-scale devices were constructed by replicating the unit cell in both in-plane directions until reaching the desired system sizes, being indicated in the main text along with the corresponding total number of atoms. Quantum transport in these devices was simulated using the TBtrans code,²⁷ which is based on an efficient implementation of the Green's function formalism. Current injection at specific sites of the device was simulated via a constant, on-site broadening self-energy in the device Green's function,¹⁴ effectively modelling a probe microscopy tip in chemical contact with one atom. Current was drained by in-plane semi-infinite hNPG electrodes along the x-direction (the GNR direction). Complex absorbing potential walls were applied along the y-direction, to avoid electronic back-reflection at the nonperiodic boundaries of each device.^{28,29} Bond transmission maps were generated using SISL to illustrate the spatial distribution of injected currents,²⁹ using a color scale proportional to the transmission magnitude at each atom, with high transmission displayed in bright yellow and low to zero transmission in dark purple (all color bars in the article span the same range of values, 0 to 0.045). Bond transmissions were computed by TBtrans at the Fermi level only. In terms of performance, the largest TBtrans device simulation presented in this work, consisting of a 1017

x 36 nm² meta-hNPG system with nearly 10⁶ atoms (968,760; 1 p_z orbital/atom), was performed using the OpenMP-parallelized TBtrans program (version 5.1-MaX-50-g4df4b742f) on a 2x10-core Intel Xeon E5-2660v3 (2.6GHz) node with 128 GB RAM, considering 20 OpenMP threads. It requires ~55 GB of RAM (memory requirements represent the main constraint for this type of simulation) and ~10 min of CPU time. Set-up and post-processing (i.e., plotting bond transmission maps) in SISL for this simulation required ~5 min and ~35 min, respectively.

Analytical model

The wave equation for the coupled modes, proposed to describe electron transport in hNPG, corresponds to the system of coupled discrete differential equations

$$\text{Eq. (1)} \quad \begin{cases} i \frac{dA_n}{dx} + \kappa(B_n + B_{n-1}) = \epsilon_A A_n, \\ i \frac{dB_n}{dx} + \kappa(A_n + A_{n+1}) = \epsilon_B B_n, \end{cases}$$

where A_n (B_n) waveguides within the n th unit cell in the y direction are associated with nGNRs (cGNRs) with a local energy shift ϵ_A (ϵ_B) and κ as the nearest neighbor coupling. We consider the weak-coupling regime, with only nearest-neighbor coupling between waveguides. We also consider the case where injection is done in a single ribbon, corresponding to a delta source at a lateral waveguide (for instance A_0) at a fixed position $\delta(x - x_0)$. Solutions $Y_n \in \{A_n, B_n\}$ can be expressed as $Y_n(x) = \int_{-\pi}^{\pi} dk e^{ikx} y_k(x)$, where k is linear momentum. Fourier transforming into ω -space allows us to rewrite the coupled differential equations in an algebraic form:

Eq. (2)

Where I is a 2x2 identity matrix, $\Omega = \begin{pmatrix} \alpha & 2t^* \cos(k/2) \\ 2t \cos(k/2) & -\alpha \end{pmatrix}$, $y(\omega) = \begin{pmatrix} a_k(\omega) \\ b_k(\omega) \end{pmatrix}$ and $t = \kappa e^{ik/2}$ being the k -dependent complex coupling.

Real-space solutions can be obtained by Fourier transformation back from (n, ω) into (n, x) :

$$\text{Eq. (3)} \quad \begin{cases} A_n(x) = -i \int_{-\pi}^{\pi} dk e^{ikx} \cos(\omega_0 x) - i \int_{-\pi}^{\pi} dk e^{ikx} \frac{\alpha}{\omega_0} \sin(\omega_0 x) \\ B_n(x) = \int_{-\pi}^{\pi} dk e^{ikx} 2t \cos(k/2) \sin(\omega_0 x) \end{cases}$$

with $\omega_0^2 = \alpha^2 + |2t \cos(k/2)|^2$.

In this work, we focus on two limiting cases. For $\alpha \ll \kappa$, solutions reduce to:

$$\text{Eq. (4)} \quad \begin{cases} A_n(x) \approx -i J_n(2\kappa x) \\ B_n(x) \approx J_{n-1}(2\kappa x) - J_{n+1}(2\kappa x) \end{cases}$$

which recovers the Talbot interference pattern of NPG.¹³ Here J_n denotes the Bessel functions of the first kind. In the opposite regime, with $\alpha \gg \kappa$, solutions become:

$$\text{Eq. (5)} \quad \begin{cases} A_n(x) \approx -i J_n\left(\frac{2\kappa^2}{\alpha} x\right) e^{-i\alpha x} \\ B_n(x) \approx \frac{2\kappa}{\alpha} \sin(\alpha x) J_n\left(\frac{2\kappa^2}{\alpha} x\right) e^{-i\alpha x} \end{cases}$$

In this case, Talbot-like interference is hosted only by A_n sub-system, with *wavenumber* rescaled by a factor $\kappa/\alpha \ll 1$, while waveguide modes intensity on B_n is suppressed accordingly. Periodic modulation of the field waveguide modes in B_n originates from the potential (propagation constant) mismatch.

Acknowledgements

G.C. acknowledges the project SAMOTHRACE “Sicilian micro and nanotechnology research and innovation centre” founded by PNRR-MUR (ECS_00000022, CUP B63C22000620005) for partial support. I.A. is grateful for a Juan de la Cierva postdoctoral grant (FJC2019-038971-I) from the Ministerio de Ciencia e Innovación. ICN2 is funded by the CERCA Programme from Generalitat de Catalunya, has been supported by the Severo Ochoa Centres of Excellence programme [SEV-2017-0706] and is currently supported by the Severo Ochoa Centres of Excellence programme, Grant CEX2021-001214-S, both funded by MCIN/AEI/10.13039.501100011033. AAM was funded by Independent Research Fund Denmark, Grant 0.46540/3103-00229B. MP acknowledges support from PID2022-139776NB-C61, funded by Spanish MCIN/AEI <https://doi.org/10.13039/501100011033>, by the ERDF, A way of making Europe, and by Generalitat de Catalunya (Grant 2021SGR01519).

Conflicts of interest

There are no conflicts of interest to declare.

Code availability

The scripts used to set up the simulations are available from the corresponding author upon reasonable request.

Bibliography

- (1) Liu, X. H.; Guan, C. Z.; Wang, D.; Wan, L. J. Graphene-like Single-Layered Covalent Organic Frameworks: Synthesis Strategies and Application Prospects. *Advanced Materials* **2014**, *26* (40), 6912–6920. <https://doi.org/10.1002/adma.201305317>.
- (2) Fan, Q.; Gottfried, J. M.; Zhu, J. Surface-Catalyzed C–C Covalent Coupling Strategies toward the Synthesis of Low-Dimensional Carbon-Based Nanostructures. *Accounts of Chemical Research* **2015**, *48* (8), 2484–2494. <https://doi.org/10.1021/acs.accounts.5b00168>.
- (3) Xing, G. Y.; Zhu, Y. C.; Li, D. Y.; Liu, P. N. On-Surface Cross-Coupling Reactions. *Journal of Physical Chemistry Letters* **2023**, *14* (19), 4462–4470. <https://doi.org/10.1021/acs.jpcclett.3c00344>.
- (4) Song, S.; Su, J.; Telychko, M.; Li, J.; Li, G.; Li, Y.; Su, C.; Wu, J.; Lu, J. On-Surface Synthesis of Graphene Nanostructures with π -Magnetism. *Chemical Society Reviews* **2021**, *50* (5), 3238–3262. <https://doi.org/10.1039/d0cs01060j>.
- (5) De Oteyza, D. G.; Frederiksen, T. Carbon-Based Nanostructures as a Versatile Platform for Tunable π -Magnetism. *Journal of Physics Condensed Matter* **2022**, *34* (44), 443001. <https://doi.org/10.1088/1361-648X/ac8a7f>.
- (6) Wang, H.; Wang, H. S.; Ma, C.; Chen, L.; Jiang, C.; Chen, C.; Xie, X.; Li, A. P.; Wang, X. Graphene Nanoribbons for Quantum Electronics. *Nature Reviews Physics* **2021**, *3* (12), 791–802. <https://doi.org/10.1038/s42254-021-00370-x>.
- (7) Saraswat, V.; Jacobberger, R. M.; Arnold, M. S. Materials Science Challenges to Graphene Nanoribbon Electronics. *ACS Nano* **2021**, *15* (3), 3674–3708. <https://doi.org/10.1021/acsnano.0c07835>.
- (8) Moreno, C.; Vilas-Varela, M.; Kretz, B.; Garcia-Lekue, A.; Costache, M. V.; Paradinas, M.; Panighel, M.; Ceballos, G.; Valenzuela, S. O.; Peña, D.; Mugarza, A. Bottom-up Synthesis of Multifunctional Nanoporous Graphene. *Science* **2018**, *360* (6385), 199–203. <https://doi.org/10.1126/science.aar2009>.

- (9) Qin, T.; Wang, T.; Zhu, J. Recent Progress in On-Surface Synthesis of Nanoporous Graphene Materials. *Communications Chemistry* **2024**, *7* (1), 154. <https://doi.org/10.1038/s42004-024-01222-2>.
- (10) Moreno, C.; Diaz de Cerio, X.; Vilas-Varela, M.; Tenorio, M.; Sarasola, A.; Brandbyge, M.; Peña, D.; Garcia-Lekue, A.; Mugarza, A. Molecular Bridge Engineering for Tuning Quantum Electronic Transport and Anisotropy in Nanoporous Graphene. *Journal of the American Chemical Society* **2023**, *145*, 8988–8995. <https://doi.org/10.1021/jacs.3c00173>.
- (11) Mutlu, Z.; Jacobse, P. H.; McCurdy, R. D.; Llinas, J. P.; Lin, Y.; Veber, G. C.; Fischer, F. R.; Crommie, M. F.; Bokor, J. Bottom-Up Synthesized Nanoporous Graphene Transistors. *Advanced Functional Materials* **2021**, *31* (47), 2103798. <https://doi.org/10.1002/adfm.202103798>.
- (12) Tenorio, M.; Moreno, C.; Febrer, P.; Castro Esteban, J.; Ordejón, P.; Peña, D.; Pruneda, M.; Mugarza, A. Atomically Sharp Lateral Superlattice Heterojunctions Built-In Nitrogen-Doped Nanoporous Graphene. *Advanced Materials* **2022**, *34* (20), 2110099. <https://doi.org/10.1002/adma.202110099>.
- (13) Calogero, G.; Papior, N. R.; Kretz, B.; Garcia-Lekue, A.; Frederiksen, T.; Brandbyge, M. Electron Transport in Nanoporous Graphene: Probing the Talbot Effect. *Nano Letters* **2018**, *19* (1), 576–581. <https://doi.org/10.1021/acs.nanolett.8b04616>.
- (14) Calogero, G.; Alcón, I.; Papior, N.; Jauho, A.-P.; Brandbyge, M. Quantum Interference Engineering of Nanoporous Graphene for Carbon Nanocircuitry. *Journal of the American Chemical Society* **2019**, *141* (33), 13081–13088. <https://doi.org/10.1021/jacs.9b04649>.
- (15) Alcón, I.; Cummings, A. W.; Roche, S. Tailoring Giant Quantum Transport Anisotropy in Nanoporous Graphenes under Electrostatic Disorder. *Nanoscale Horizons* **2024**, *9*, 407–415. <https://doi.org/10.1039/D3NH00416C>.
- (16) Calogero, G.; Alcón, I.; Kaya, O.; Papior, N.; Cummings, A. W.; Brandbyge, M.; Roche, S. Robust Quantum Engineering of Current Flow in Carbon Nanostructures at Room Temperature. *Carbon* **2025**, *234*, 119950. <https://doi.org/10.1016/j.carbon.2024.119950>.
- (17) Abbas, G.; Sonia, F. J.; Jindra, M.; Červenka, J.; Kalbáč, M.; Frank, O.; Velický, M. Electrostatic Gating of Monolayer Graphene by Concentrated Aqueous Electrolytes. *J. Phys. Chem. Lett.* **2023**, *14* (18), 4281–4288. <https://doi.org/10.1021/acs.jpcllett.3c00814>.
- (18) Abbas, G.; Sonia, F. J.; Jindra, M.; Červenka, J.; Kalbáč, M.; Frank, O.; Velický, M. Electrostatic Gating of Monolayer Graphene by Concentrated Aqueous Electrolytes. *J. Phys. Chem. Lett.* **2023**, *14* (18), 4281–4288. <https://doi.org/10.1021/acs.jpcllett.3c00814>.
- (19) Perdew, J. P.; Burke, K.; Ernzerhof, M. Generalized Gradient Approximation Made Simple. *Physical Review Letters* **1996**, *77* (18), 3865–3868. <https://doi.org/10.1103/PhysRevLett.77.3865>.
- (20) Soler, J. M.; Artacho, E.; Gale, J. D.; García, A.; Junquera, J.; Ordejón, P.; Sánchez-Portal, D. The SIESTA Method for Ab Initio Order-N Materials Simulation. *Journal of Physics: Condensed Matter* **2002**, *14* (11), 2745–2779. <https://doi.org/10.1088/0953-8984/14/11/302>.
- (21) Papior, N.; Febrer, P. Sisl, 2024. <https://doi.org/10.5281/zenodo.14357951>.
- (22) Alcón, I.; Calogero, G.; Papior, N.; Brandbyge, M. Electrochemical Control of Charge Current Flow in Nanoporous Graphene. *Advanced Functional Materials* **2021**, *31* (40), 2104031. <https://doi.org/10.1002/adfm.202104031>.
- (23) Calogero, G.; Papior, N.; Koleini, M.; Larsen, M. H. L.; Brandbyge, M. Multi-Scale Approach to First-Principles Electron Transport beyond 100 Nm. *Nanoscale* **2019**, *11*, 6153–6164. <https://doi.org/10.1039/C9NR00866G>.
- (24) Alcón, I.; Papior, N.; Calogero, G.; Viñes, F.; Gamallo, P.; Brandbyge, M. Acetylene-Mediated Electron Transport in Nanostructured Graphene and Hexagonal Boron Nitride. *The Journal of Physical Chemistry Letters* **2021**, *12*, 11220–11227. <https://doi.org/10.1021/acs.jpcllett.1c03166>.

- (25) Alcón, I.; Calogero, G.; Papior, N.; Antidormi, A.; Song, K.; Cummings, A. W.; Brandbyge, M.; Roche, S. Unveiling the Multiradical Character of the Biphenylene Network and Its Anisotropic Charge Transport. *Journal of the American Chemical Society* **2022**, *144* (18), 8278–8285. <https://doi.org/10.1021/jacs.2c02178>.
- (26) Diaz de Cerio, X.; Bach Lorentzen, A.; Brandbyge, M.; Garcia-Lekue, A. Twisting Nanoporous Graphene on Graphene: Electronic Decoupling and Chiral Currents. *Nano Lett.* **2025**, *25* (4), 1281–1286. <https://doi.org/10.1021/acs.nanolett.4c04262>.
- (27) Papior, N.; Lorente, N.; Frederiksen, T.; García, A.; Brandbyge, M. Improvements on Non-Equilibrium and Transport Green Function Techniques: The next-Generation Transiesta. *Computer Physics Communications* **2017**, *212*, 8–24. <https://doi.org/10.1016/J.CPC.2016.09.022>.
- (28) Xie, H.; Kwok, Y.; Jiang, F.; Zheng, X.; Chen, G. Complex Absorbing Potential Based Lorentzian Fitting Scheme and Time Dependent Quantum Transport. *The Journal of Chemical Physics* **2014**, *141* (16), 164122. <https://doi.org/10.1063/1.4898729>.
- (29) Calogero, G.; Papior, N. R.; Bøggild, P.; Brandbyge, M. Large-Scale Tight-Binding Simulations of Quantum Transport in Ballistic Graphene. *Journal of Physics: Condensed Matter* **2018**, *30* (36), 364001. <https://doi.org/10.1088/1361-648X/aad6f1>.